JOURNAL OF PROPULSION AND POWER
Vol. 11, No. 5, September–October 1995

Flow-Structural Interaction Inside a Solid Rocket Motor During Ignition Transient

W. A. Johnston* and J. W. Murdock†
The Aerospace Corporation, Los Angeles, California 90009

In this article, a numerical procedure for the analysis of the flow-structural interaction inside a solid rocket motor (SRM) is developed from existing codes. This computer code simultaneously models the developing flowfield and the associated propellant grain deformation during the ignition transient period of SRM operation. It was created by coupling together an ignition-transient flow code, which provides a detailed picture of the time-dependent flowfield and flame spreading inside the motor, with a set of structural influence coefficients, which enable us to calculate the grain deformation that results from a given surface pressure distribution. Also included in the numerical package is a grid-generation code, which generates a grid mesh for the internal-flow passages, based on the deformed shape of the propellant grain. This grid mesh then is used in the ignition transient flow code. As these three component calculations march forward in time, they interact continuously; in this way the flowfield and grain shape are updated continuously. The computer analysis was validated by and used to study the static test failure of the Titan solid rocket motor upgrade (SRMU) that occurred on April 1, 1991 at Edwards Air Force Base. It has since been used to predict the stability of other motors.

I. Introduction

THE static test failure of the Titan solid rocket motor upgrade (SRMU) that occurred on April 1, 1991 at Edwards Air Force Base resulted in activity at various facilities to model the test. This activity included the present work, as well as Refs. 1 and 2. Reference 1 is a transient approach with a very simplified geometry. Reference 2 is a quasisteady flow model. The approach reported herein is transient and makes minimal geometric approximations.

During the ignition transient period of solid rocket motor (SRM) operation, several complex, time-dependent processes advance in a strongly coupled manner. For example, in a large segmented SRM, the hot gas from the igniter travels down the bore and heats the propellant surface to ignition; once this ignition occurs, the propellant surface becomes a site of gas generation. Since the convective and radiative heat transfer that lead to propellant ignition are strongly dependent on the developing flowfield, and since the development of the internal-flowfield is strongly dependent on the rate at which the flame spreads down the motor, it is obvious that the time-dependent flow and surface temperature are closely coupled. Furthermore, the surface pressure load that develops on the propellant segments causes the segments to deform, which in turn alters the flowfield. This results in the additional coupling of the internal-flowfield with the propellant geometry. This flow-structural coupling is particularly important in segmented SRMs, when the propellant segments have forward corners (see Fig. 1) that jut out into the bore at intersegment slots (e.g., Titan 5, 5-1/2, 7 segment SRMs, Space Shuttle SRM, Titan SRM upgrade). When a protruding corner is subjected to an axial flow, the surface pressure deforms the corner out into the bore and further constricts the flow, which then raises the upstream pressure and exacerbates the pressure loading on the corner. If this feedback loop proves to be unstable, then the corner will continue to deform and the motor to pressurize, until either the grain or the motor case fails.[3]

In this article, a numerical procedure for the analysis of the flow-structural interaction is presented. This computer code simultaneously models the developing flowfield and the associated propellant grain deformation during the ignition transient period of SRM operation. It is during this initial period of motor operation, when the propellant surface has receded only a little through burning and erosion, that the pressure differential across propellant segment corners typically is at a maximum and the bore radius at a minimum. It is at this time that the interaction between the grain and the flowfield, and the associated danger of grain and motor case failure, is greatest. This code, which is designed to provide a model of the time-dependent, fluid–solid interaction inside an SRM, was created by coupling together the following:

1) An ignition transient flow code,[4] which provides a detailed picture of the time-dependent flowfield and flame spreading inside the motor. The ignition transient flow code is itself created by coupling together an unsteady internal-flow code[5] with an unsteady heat conduction solution for the propellant surface temperature.

2) A set of structural influence coefficients, which enable us to calculate the major features of the grain deformation that result from a given surface pressure distribution.[6]

3) A grid-generation code, which generates a grid mesh for the internal-flow passages, based on the deformed shape of

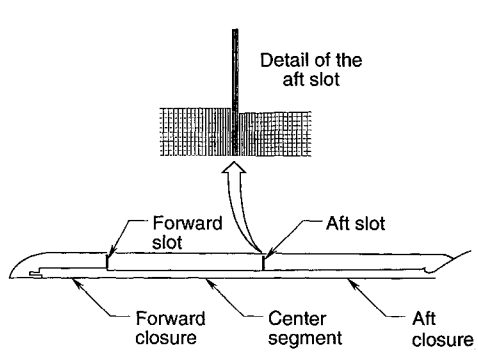

Fig. 1 Initial geometry and cell mesh for the Titan SRMU internal flowfield.

Received Nov. 1, 1993; revision received June 9, 1994; accepted for publication Oct. 26, 1994. This paper is declared a work of the U.S. Government and is not subject to copyright protection in the United States.

*Member of the Technical Staff. Member AIAA.

†Manager, Fluid Mechanics Technology Section. Associate Fellow AIAA.

the propellant grain. This grid mesh then is used in the ignition transient flow code.

As these three component calculations march forward in time, they interact continuously; in this way, the flowfield and grain shape are updated continuously.

The computer code was applied to the analysis of the static test failure of the SRMU. Numerical results from several SRMU ignition transient simulations with different propellant moduli are presented and compared with the measured head- and aft-end chamber pressures that were obtained during the static test firing.

II. Theory

As discussed in the Introduction, the numerical procedure developed and used in this work has three main components: 1) an ignition transient flow solution, 2) a propellant grain deformation calculation based on a set of structural influence coefficients, and 3) a grid-generation code. The component parts of this time-dependent, coupled, flow-structural interactive calculation are discussed separately.

A. Ignition Transient Flow Solution

The numerical calculation procedure for the ignition transient flowfield has been described in detail[4]; here, we present only a brief description of that procedure. The ignition transient flow solution is itself best described as a composite calculation. The approach was to combine an unsteady, axisymmetric solution of the equations of inviscid fluid motion with semi-empirical models for the convective and radiative heat transfer to the propellant surface during the run-up to ignition. The inviscid, single-phase, single-component flow solution consists of a time-marching, finite volume solution of the Euler equations. This flow solution, which is spatially second-order accurate and employs the total variation diminishing (TVD) methodology of Harten,[7] has been described[8] and implemented for segmented SRMs.[5] An unsteady, one-dimensional, heat conduction solution for the propellant grain is coupled to this flow solution in order to calculate the propellant surface temperature. Together with a surface temperature ignition criterion, this determines the ignition delay and flame spreading rate.

A portion of the finite volume cell mesh used in an SRM ignition transient simulation is shown in Fig. 1. (Because the flow is approximated as axisymmetric, only the upper half of the motor is displayed.) The grid covers the central bore from the head-end of the motor to a small distance downstream of the nozzle throat. The grid also resolves the slot regions that lie between propellant segments. In the absence of the flow-structural interaction, the ignition transient flow solution proceeds as follows. Initially, the gas in the motor chamber is at ambient conditions and at rest. The hot gas from the igniter (the outline of which may be found in Fig. 1, on the centerline at the head end of the motor) begins to emerge from the igniter port(s) at time zero and to enter the computational domain. This gas travels down the bore and, in so doing, heats the propellant surface area elements that it passes. As each surface area element reaches the autoignition temperature, it is deemed to burn and acts throughout the remainder of the calculation as an inflow boundary element that injects hot combustion gas into the computational domain. As successive surface elements are "turned on" by the hot gas that moves through the motor, the flame spread is simulated. Rather early in this process, the nozzle chokes and a period of rapid motor pressurization begins. This pressurization continues throughout the period of flame spreading and beyond, until a steady-state situation appears after some elapsed time, typically on the order of 0.5 s for a large segmented SRM. Since the ignition transient code (in the absence of the flow-structural interaction) runs on a fixed grid geometry, the calculation will converge on a steady-state result, although in an actual motor there is a continuing change in propellant surface location due to pressure deformation and burnback. Therefore, in an actual SRM, the flow pattern at the end of the ignition transient period is only quasisteady at best. If the propellant deformation is both rapid and severe, the resulting flow will be unsteady.

B. Grain Shape Calculation

The grain deformation component in this flow-structural interactive calculation procedure is first activated after a specified number of flow solution time steps have been completed; this continues at similar intervals throughout the time-marching process. An interval of 100 time steps between geometry updates, which was found by experience to be both sufficiently time-accurate and economically feasible, was used in the calculations. Since the typical flow solution time step was limited by numerical stability to the order of 10^{-5} s, it follows that the grain shape was recalculated about every millisecond. The grain deformation calculation itself consists of multiplying (for each propellant segment under consideration) a pressure loads vector by a structural influence coefficient matrix to get the resultant displacements at a few key points, which define the shape of the grain. Consider Fig. 2, where this procedure is illustrated. The quantity E is the propellant modulus (MPa); P_1, P_2, P_3, P_4, and P_5 are the values of the depicted pressure loads (MPa); Δr_A, Δr_B, Δr_C, Δz_A, and Δz_C are the radial and axial displacements (mm) of points A, B, C, which are at the corners and midpoint of the segment. These structural influence coefficients were supplied to us by Patel and Yang[6]; the coefficients were obtained from a series of grain structural analyses carried out using the ABAQUS code.[9] In these analyses, the propellant is treated as an isotropic, homogeneous, linear elastic material. Figure 2 shows the structural influence coefficient matrix used for the Titan SRMU center propellant segment. The corresponding information for the Titan SRMU aft propellant segment is shown in Fig. 3. Note that although the coefficient matrices used herein are relatively small, there is no fundamental limitation on size. The choice here was dictated primarily by a desire to be consistent with our grid-generation approximations. The deformation of the forward propellant segment, which plays no role in the flow-structural interaction, is not considered in our calculation. Consider how the grain deformation calculation functions within the context of the flow-structural interactive procedure. After 100 flow solution time steps have been completed, values of the pressure loads P_{1-5} are calculated. Our previous experience with internal-flow solutions for the SRMU geometry indicated that the actual surface pressure distribution on the propellant segments could be approximated accurately by a composite of these simple loads. Once these pressure loads have been obtained, a matrix multiplication gives the displacements of the key points. The locations of these points are adjusted further

$$\begin{bmatrix} \Delta r_A \\ \Delta z_A \\ \Delta r_B \\ \Delta r_C \\ \Delta z_C \end{bmatrix} = \frac{1}{E} \begin{bmatrix} 664.665 & -213.586 & 43.017 & -681.949 & 2.449 \\ 761.528 & -119.530 & 162.560 & -839.800 & 10.274 \\ 111.440 & -0.373 & 51.920 & -35.517 & -29.548 \\ 692.061 & 0.028 & 629.117 & 2.664 & -694.017 \\ -794.794 & -0.010 & -613.461 & -10.551 & 850.900 \end{bmatrix} \begin{bmatrix} P_1 \\ P_2 \\ P_3 \\ P_4 \\ P_5 \end{bmatrix}$$

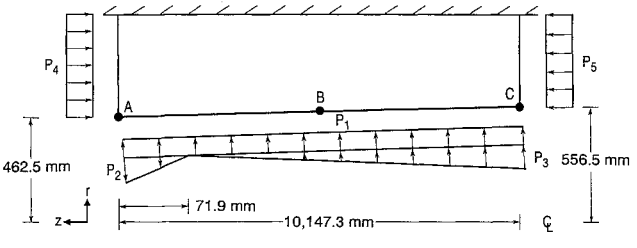

Fig. 2 Structural influence coefficients for the center propellant segment, Titan SRMU (initial geometry).

$$\begin{Bmatrix} \Delta r_A \\ \Delta z_A \\ \Delta r_B \end{Bmatrix} = \frac{1}{E} \begin{pmatrix} 685.538 & -194.376 & 52.573 & -686.516 & 231.231 \\ 805.881 & -110.236 & 193.040 & -849.259 & 403.428 \\ 69.042 & -0.272 & 28.567 & -28.362 & 4.402 \end{pmatrix} \begin{Bmatrix} P_1 \\ P_2 \\ P_3 \\ P_4 \\ P_5 \end{Bmatrix}$$

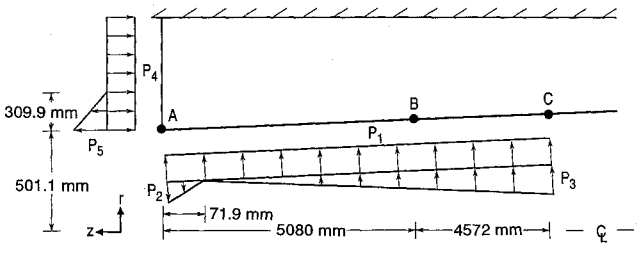

Fig. 3 Structural influence coefficients for the aft propellant segment, Titan SRMU (initial geometry).

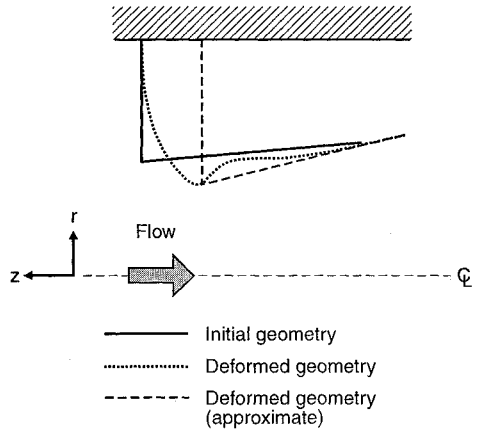

Fig. 4 Actual and approximate deformed grain surfaces at the forward corner of the aft and center segments, Titan SRMU.

to account for propellant burnback, at an assumed rate of 7.6 mm/s. When these points have been relocated in this manner, the deformed surface shape is approximated by straight line segments. Based on our observations of the actual surface shape that a structural analysis code such as ABAQUS[9] predicts for a deformed grain segment, this line segment shape is a good approximation over most of the propellant surface. However, it is only a fair approximation at the forward corners of the aft and center segments, where the surface exhibits larger curvature. A further approximation is made in these slot regions, i.e., that propellant surfaces in the slots must be purely radial; this additional constraint is imposed by the grid-generation procedure that we have yet to discuss. The situation is depicted in Fig. 4. We shall return to a discussion of these geometric approximations later. Once this updated polygonal grain segment shape is obtained, then a new finite volume grid is generated for the flow passages, and the flow solution is marched forward in time for another 100 steps.

C. Grid Geometry

The initial grid geometry for the Titan SRMU in the vicinity of the aft slot is shown in Fig. 1. The complete axisymmetric grid mesh contains 3545 cells. In the actual SRMU, the propellant in the forward closure has a star-grain cross section with axial grooves. (A more complete description of the internal geometry of the SRMU may be found in Ref. 10.) To account for this three-dimensional feature in our axisymmetric model, we omit the axial grooves, which results in an annular propellant cross section, and set the inner radius of this annulus so that the void volume in the actual forward segment and computational forward segment are matched. Then the burning rate in the forward closure is adjusted upward to account for any discrepancy in the burning area. The actual SRMU has two other features that have been omitted in the interest of simplicity. First, the actual SRMU geometry includes a submerged nozzle, which does not appear in the computational geometry. This geometric omission is accounted for by an enhanced burning rate over a small portion of the burning surface in the aft closure, where this submerged region is located. Second, in the actual SRMU, there are stress relief grooves that appear as small indentations in the grain surface near the top of the slots. These features also are omitted from the computational geometry and modeled with a locally enhanced burning rate. Note that these two features are omitted from the geometry of the flow solution, but were included in the grain structural analyses that yielded the influence coefficients.

The grid-generation scheme that creates the initial cell mesh, and all of the subsequent cell meshes during the course of the time-marching interactive calculation, is a modified version of a code described in Ref. 11. An important feature of the numerous grids generated during the interactive calculation is that the number of flowfield cells does not change, and that they retain their relative positions within the mesh as that mesh undergoes distortion. When a geometry update is carried out, the shape and position of many cells will change slightly. Since our geometry updates are performed quite frequently, compared to the grain deformation rates we have encountered, the change in a cell's shape and location from an update typically is very small. For this reason, we simply carry over the cell values of pressure, density, temperature, and velocity during the geometry update process. The grid-generation procedure is economical (less than 3 CPU s of run time on a Cray X-MP-14 for the grid in Fig. 1), but it is limited to grids where the vertical borders between cells are strictly radial lines. As noted previously, this constraint necessitates some additional approximation of the deformed grain surface, after that surface shape is calculated. However, it is important to note that since the flow-structural interactive calculation described here is constructed in modular form, it would be possible to replace the present geometry module with something more general. Hence, this limitation is not inherent in the overall interactive scheme.

III. Numerical Results

In this section, results from several numerical simulations using the time-dependent, flow-structural interactive procedure are presented. We begin with a discussion of the static firing of the Titan SRMU, which occurred on April 1, 1991 at Edwards Air Force Base. At about 1.6 s into this static test, the motor case failed due to excessive internal pressure. Chamber pressure measurements obtained just prior to the failure showed the head-end chamber pressure increasing rapidly and the aft-end pressure dropping. This divergence of the head-end and aft-end chamber pressures implies a bore constriction, and strain gauge measurements from various axial locations placed this critical constriction at the aft slot. The probable cause of this bore constriction was judged to be the uncontrolled deformation, or collapse, of the forward corner of the aft propellant segment under the applied pressure load. Due to the uncertainty in the value and behavior of the propellant modulus, and the crucial role that this property plays in the success or failure of the motor, our approach was to perform numerical static firing simulations for a range of propellant moduli. Our goal was to see if a reasonable depiction of this failure scenario could be achieved with some reasonable value of the modulus. We present results from simulations with the modulus represented as a decreasing function of time and with constant modulus. The first type of behavior was intended to represent a relaxation modulus. In the interest

of simplicity, we have replaced the usual decreasing exponential behavior[12] with a decreasing linear behavior. The assumed modulus functions for the four cases considered here are shown in Fig. 5. Lightweight analog motor tests carried out by Hercules[13] have been analyzed to determine the modulus. We computed E to be 8.6 MPa at 0.4 s, dropping to 6.8 MPa at 2 s with an accuracy of ±20%. Thus, cases I, II, and IV are within the estimated uncertainty range of the modulus, while case III is well above this range.

The various gas and propellant properties common to all the SRMU simulations are found in Table 1, and the igniter mass flow rate used in these calculations[14] is shown in Fig. 6. Note that although the geometric surface recession is approximated as constant, the local mass flux from the burning surface is correctly computed as a function of pressure. Also, we have attempted to model the burning rate reduction factor (i.e., the so-called "hump factor"[15]) that solid propellants exhibit immediately after ignition. We model this phenomenon by starting all simulations with a burning rate that is 2% less than the nominal value and allow the burning rate to rise linearly to the nominal value (8.00 mm/s) during the first 1.5 s. A typical SRMU simulation required about 5 h of CPU time on the Cray X-MP-14 to reach 1 s of physical time and about 1 MWord of storage for the grid mesh previously described.

Table 1 Gas and propellant properties, Titan SRMU

Specific heat ratio γ	1.13
Gas constant R, J/[kg·K]	282.6
Flame temperature T_{flame}, K	3537
Ignition temperature T_{ignition}, K	700
Propellant density ρ_{prop}, mg/m^3	1.79
Burning rate constant C, mm/s	8.00
Burning rate exponent n	0.30
Propellant thermal diffusivity α, μm^2/s	31.8
Prandtl number Pr	0.45
Propellant thermal conductivity k, W/[m·K]	0.692
Gas viscosity μ_{ref}, μPa·s	0.314

$\mu = \mu_{\text{ref}}(T/0.556)^{0.65}$ with T in K and burning surface mass flow rate (kg/m^2·s) = $\rho_{\text{prop}}C(p/6.89)^n$ with p in MPa.

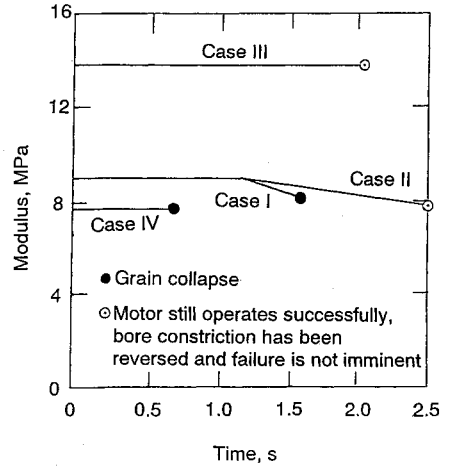

Fig. 5 Modulus functions for Titan SRMU simulations, cases I–IV.

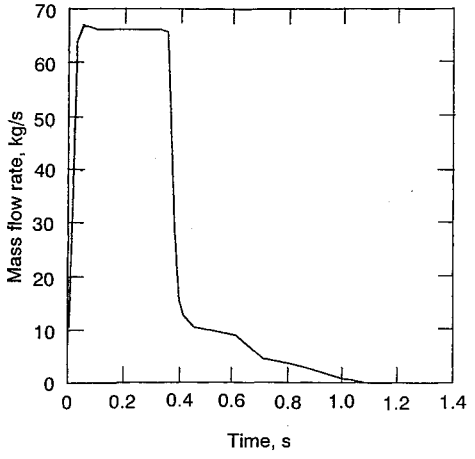

Fig. 6 Igniter mass flow rate, Titan SRMU.

A. Case I

As a first case, we consider an SRMU characterized by the following propellant modulus:

$$E = \begin{cases} 9.0 & t \le 1.1 \\ 9.0 - 1.7(t - 1.1) & t > 1.1 \end{cases}$$

where E is in MPa and t in seconds. The computed head- and aft-end chamber pressures are compared with static firing data in Fig. 7. The computed bore radii at the forward and aft corners of the center and aft propellant segments are shown in Fig. 8.

It is instructive to consider in detail the time-dependent situation inside the motor. The simulation starts at $t = 0$, with the gas inside the motor at ambient conditions and at rest, and with the propellant segments in their initial shape. At this time the igniter begins to function, and hot gas begins to emerge from the axial igniter port and flow down the bore. The first propellant surface ignition occurs at about $t = 0.09$ s near the forward slot, and from this point flame spreads down the bore toward the nozzle and up the bore toward the top of the motor. The nozzle chokes at about $t = 0.105$ s, and the steep rise in chamber pressure begins (see Fig. 7). Since the rising flow rate implies an increased propellant loading, especially on forward facing corners, we begin to see an

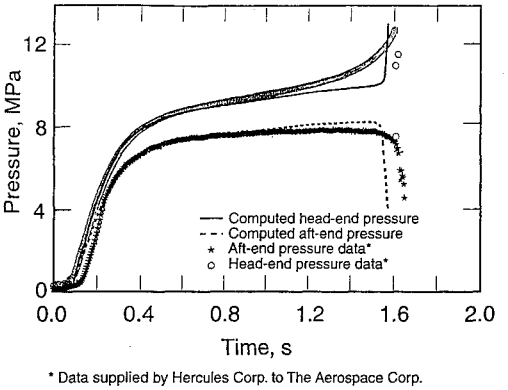

* Data supplied by Hercules Corp. to The Aerospace Corp.

Fig. 7 Comparison of computed (case I) and measured head- and aft-end pressures, Titan SRMU.

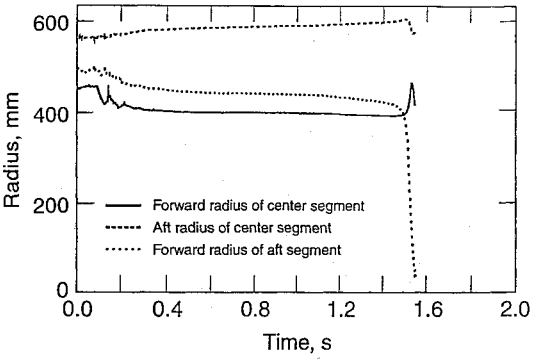

Fig. 8 Computed bore radii (case I), Titan SRMU.

increase in the amount of propellant deformation at this time (see Fig. 8). For the period from approximately $t = 0.1$ to $t = 0.3$ s, the rate of deformation is rather "choppy," due to significant pressure wave action during this time (i.e., pressure waves traveling up and down the motor). Although in some computations with the code these grain oscillations have not decayed (presumably due to the massless propellant model), in the present case, both the wave action and the grain oscillation diminish when the pressure rise begins to slow at about $t = 0.3$ s as the motor begins to settle into a quasisteady behavior. During the period from $t = 0.1$ to $t = 0.2$ s, there is a disagreement between the data and the computed aft-end pressure. We attribute this discrepancy to the fact that the pressure transducer in question was situated behind the motor insulation in the submerged nozzle region and may have exhibited a slower response for this reason. The flame spread continues from first ignition, with the flame reaching the nozzle at $t = 0.14$ s and completely penetrating the aft slot at $t = 0.20$ s, at which point the entire propellant surface has been ignited.

During the time interval from $t = 0.4$ s to $t = 1.4$ s, changes in the flowfield and propellant continue to occur, but at a much more gradual pace. The head- and aft-end chamber pressures continue to rise, even after the initial pressurization is complete, due to the decreasing hump factor and the increasing burning area as a result of propellant burnback. The pressure difference between the head and aft ends of the motor also continues to grow, due to the continuing drop in the bore radii at the forward corners of the segments. There are two competing effects that together set the rate at which the bore constriction proceeds. First, the deformation of the forward corners of the propellant segments, due to the applied pressure loads, causes the corners to move radially inward and to constrict the bore. Second, propellant burnback causes the corners to recede radially and to open the bore. During the time interval from 0.4 to 1.4 s, the bore radii at the front corners of the center and aft segments are slowly but inexorably decreasing, because deformation dominates the situation here. However, the aft corner of the center segment recedes, because the burnback and the deformation both act to increase the bore radius. Starting at about 1.0 s, the computed values of the head and aft pressure begin to diverge somewhat from the data, and the computed head-to-aft-end pressure differential grows more slowly than the measurements indicated. This implies that the simulation increasingly underpredicts the amount of bore constriction during this time period. We shall return to discuss this point later, but for the moment we simply note the discrepancy.

When the calculation passes $t = 1.5$ s, the situation again becomes highly unsteady. The calculation shows the head-end pressure rising sharply, and the aft-end pressure plummeting, in a manner consistent with the data. (Note that the final three values of head-end pressure data, which correspond to the motor case failing, should be omitted from comparisons with the numerical solution.) The reason for the sudden divergence of the two numerical pressure curves in Fig. 7 is apparent from Fig. 8, which shows a steep drop in the forward radius of the aft segment. This sudden, catastrophic bore constriction produces a highly unsteady internal flow; these rapid changes in the flow pattern produce some erratic behavior at the forward and aft corners of the center segment (see Fig. 8). As this bore constriction becomes extreme, the demands placed on our grid-generation procedure overwhelm the calculation, and the numerical solution fails. We note, for the purpose of comparison with other cases presented later, that the solution terminates at $t = 1.57$ s, at which time $E = 8.15$ MPa.

We have presented this particular case first, because it shows the best agreement with the experimental data, and because this relatively good agreement indicates that our numerical procedure is capable of replicating the major features of the data. We shall now consider some other propellant modulus functions that lead to motor performance histories that are qualitatively different from the present case.

B. Case II

As a second case, we consider an SRMU characterized by the propellant modulus:

$$E = \begin{cases} 9.0 & t \leq 1.1 \\ 9.0 - 0.7(t - 1.1) & t > 1.1 \end{cases}$$

Note from Fig. 5 that this modulus is slightly higher than the case I modulus. Computed head- and aft-end chamber pressures are compared with static firing data in Fig. 9, and computed bore radii are shown in Fig. 10. The purpose in displaying simulation results for this particular modulus function is that this modulus function, while very close to the modulus of case I (see Fig. 5), leads to a stable motor. In this case, the modulus drops a bit more slowly than in case I for $t > 1.1$ s, with the result that the inward deformation at the critical forward corners of the segments first slows, and then propellant burnback reverses the bore constriction. By comparing Figs. 9 and 10 with Figs. 7 and 8, one finds that these two simulations proceed in a very similar manner until $t = 1.5$ s. At this point, the case I simulation experiences a catastrophic bore constriction, while the case II motor continues to operate successfully. The reason for the success of the case II motor is found in Fig. 10, although it is somewhat difficult to discern there. While the radius of the forward corner of the aft segment decreases continually in case I, this radius reaches a minimum value of 436 mm at $t = 1.53$ s in case II and increases thereafter. In case II, the radius of the forward corner of the center segment reaches a minimum value of 399 mm at $t = 1.38$ s. The calculated head-end chamber pressure reaches a maximum at $t = 1.93$ s and then declines.

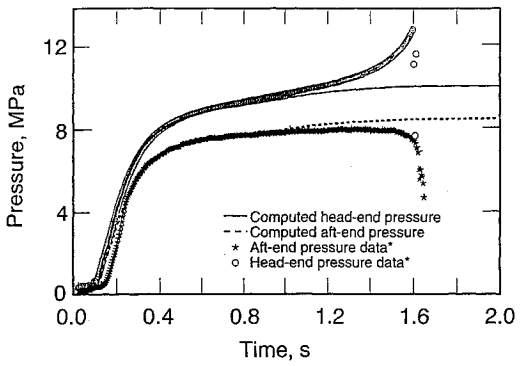

* Data supplied by Hercules Corp. to The Aerospace Corp.

Fig. 9 Comparison of computed (case II) and measured head- and aft-end pressures, Titan SRMU.

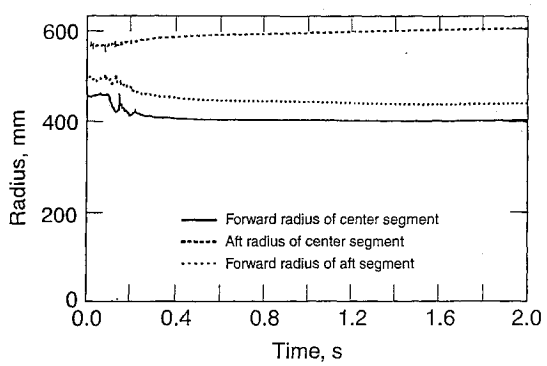

Fig. 10 Computed bore radii (case II), Titan SRMU.

The case II numerical simulation was run for 2.5 s, at which point the calculation was terminated. The numerical results at this time showed the bore widening, the chamber pressure dropping, and the motor continuing to operate successfully, even though the modulus had dropped to a value (E = 8.00 MPa) that was lower than the final value in case I. The results suggest that motor failure due to bore constriction has been avoided. Although the continued use of this linear modulus function eventually might lead to some kind of failure, the numerical results indicate that this would not happen until the modulus drops to some unrealistically low value.

C. Case III

As a third case, we consider an SRMU with a constant propellant modulus of E = 14 MPa. Computed head- and aft-end chamber pressures are compared with static firing data in Fig. 11, and computed bore radii are shown in Fig. 12. In this case, the modulus is much higher than in either of the previous two cases, and the propellant deformation is much less. It is apparent from very early in this simulation that a bore constriction failure cannot occur; both the bore radii at the forward corners of the segments are increasing after t = 0.60 s. The numerical simulation was terminated at t = 2.0 s.

The numerical results in case III support the commonsensical notion that as we move away from the modulus function of case II towards a higher modulus (i.e., a stiffer propellant), the possibility of a bore constriction failure is eliminated quickly.

D. Case IV

As a fourth case, we consider an SRMU with a constant propellant modulus of E = 7.6 MPa. Computed head- and aft-end chamber pressures are compared with static firing data in Fig. 13, and computed bore radii are shown in Fig. 14. The low modulus used in this simulation produces a catastrophic bore constriction that has many of the same characteristics as in case I. In particular, we direct the reader's attention to the sudden divergence of the computed head- and aft-end chamber pressure (Fig. 13) and the behavior of the segment corner radii during the period of pressure wave action (from 0.1 to 0.3 s) and at the time of the failure (Fig. 14). However, the case IV failure occurs much earlier. The numerical results in case IV indicate that, as we move away from the modulus function of case I toward a lower modulus (i.e., a softer propellant), a bore constriction failure increasingly is assured.

E. Additional Results

Since the propellant modulus is a quantity over which the designer may have only limited control, it is important not to rely solely on a high-modulus propellant for the success of a motor. For this reason, we have considered some propellant grain shape changes for the SRMU, which were intended to make the successful operation of the motor less sensitive to the modulus. Since the problem arises when forward corners of propellant segments jut out into the bore flow, designs that remove or mitigate this feature will produce a safer motor from the standpoint of catastrophic bore constriction. One way to achieve this would be to reverse the direction of the center propellant segment (i.e., install this segment in the motor upside down).[16] A second approach would be to chamfer (i.e., either chop off or round) the forward corners of the segments. The chamfering concept is depicted in Fig. 15.

We have carried out a flow-structural interactive simulation for an SRMU with a straight chamfer at the forward corner of the aft segment, but with the center segment unchanged. This chamfer, which removes a triangular cross-sectional piece from the corner, is drawn to scale in Fig. 15. The numerical solution for this grain design required the generation of a new set of structural influence coefficients for the aft segment, which again were supplied by Patel and Yang.[6] It is not our intention to discuss the details of this numerical solution,

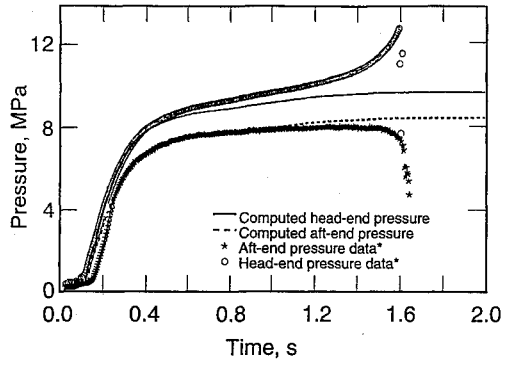

* Data supplied by Hercules Corp. to The Aerospace Corp.

Fig. 11 Comparison of computed (case III) and measured head- and aft-end pressures, Titan SRMU.

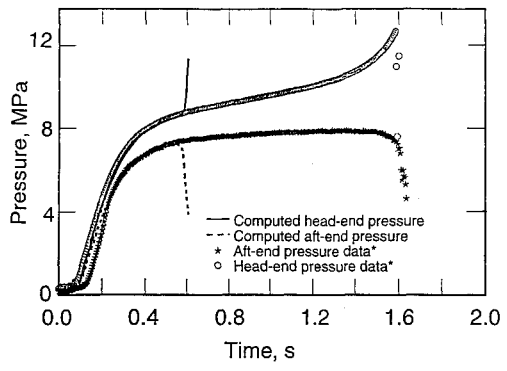

* Data supplied by Hercules Corp. to The Aerospace Corp.

Fig. 13 Comparison of computed (case IV) and measured head- and aft-end pressures, Titan SRMU.

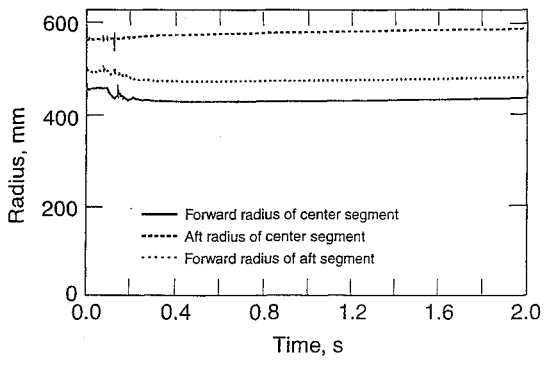

Fig. 12 Computed bore radii (case III), Titan SRMU.

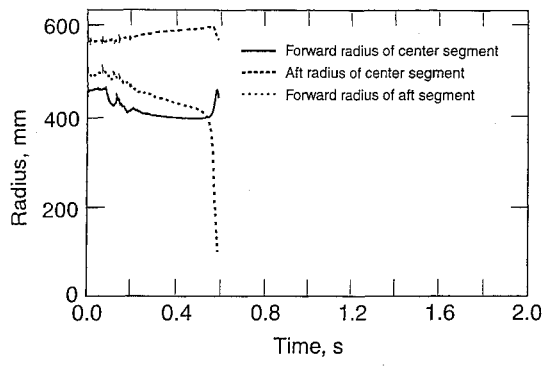

Fig. 14 Computed bore radii (case IV), Titan SRMU.

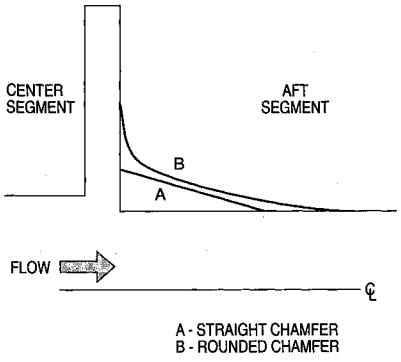

Fig. 15 Chamfering concepts for the Titan SRMU.

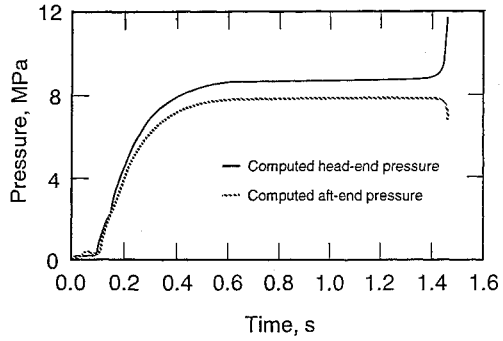

Fig. 16 Computed head- and aft-end pressures, Titan SRMU, straight chamfer on aft segment.

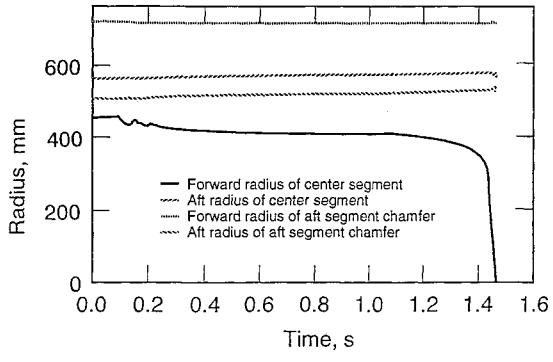

Fig. 17 Computed bore radii, Titan SRMU, straight chamfer on aft segment.

except to note that the modulus was somewhat lower than the case IV modulus and the solution predicted a motor failure; the results from this numerical solution may be found in Figs. 16 and 17. However, this failure was interesting, because in this case the catastrophic bore constriction occurred at the forward corner of the center segment (see Fig. 17). The grain deformation of the aft segment was diminished considerably by the chamfer, and the numerical results indicated that a failure originating at the aft segment would not be possible for this motor. It can be seen in the case I and case IV simulations that, while the preferred failure site for the SRMU motor is the forward corner of the aft segment, the forward corner of the center segment also has experienced a significant inward deflection. Apparently, the failure at the aft segment in these two cases may have masked an imminent failure at the center segment. There is an additional implication that a successful redesign requires chamfering both the aft and center segments.

Finally, we have carried out some steady internal-flow solutions for an SRMU with rounded chamfers, such as the one depicted in Fig. 15, at the forward corners of the aft and center segments. We have not attempted any direct comparison of the rounded chamfer design with the straight chamfer design, although it is reasonable to expect that the absence of vestigial corners makes the rounded chamfer a slightly better approach. This steady-flow solution was achieved simply by turning off the structural and geometry recalculation components of the flow-structural interactive code and running the time-marching calculation to steady state; a similar steady internal-flow solution for the nominal (unchamfered) SRMU also was run for comparison. The purpose of these two steady solutions was to make a quick assessment of the effect of this chamfer on the pressure differential around the forward corners of the aft and center segments. This pressure drop, between the slot surface of a propellant segment and the bore surface just downstream of the slot, is responsible for the inward deflection of the forward corners of the aft and center segments; the effect of the chamfers was to significantly reduce these pressure differences. The numerical results indicated that a bore constriction failure originating at either the aft or center segment would not be possible for this redesigned SRMU, unless the propellant modulus was far below any of the modulus functions used in cases I–IV. Finally, we note that as of the date of this paper, five redesigned SRMUs have been test fired successfully with rounded grain chamfers on both the center and aft segments.

IV. Discussion

In this article, we have presented a flow-structural interactive calculation procedure that was constructed for the analysis of the developing flowfield and the associated propellant deformation inside an SRM during the ignition transient period. We have applied this computer code to the simulation of the April 1991 static firing failure of the Titan SRMU and have examined the motor's performance for four different assumed propellant modulus functions, one of which (case I) produced a chamber pressure history that agreed fairly well with the data. This case I numerical solution exhibited a catastrophic bore constriction at the front corner of the aft segment that confirmed the postulated failure scenario. We believe that the code has captured the major features of this particular failure process and has done so with reasonable accuracy.

Although the code in its present form has performed well, there are two obvious areas that warrant further attention. First, the isotropic, homogeneous, linear elastic behavior we have assumed for the propellant is an idealization, the adequacy of which deserves further examination. Second, there are certain limitations on the generality of our flowfield grid-generation scheme, which we already have noted could be removed by upgrading the grid-generation component. While we are engaged in a discussion of possible improvements in the code, it is appropriate to return to the discrepancy between the data and computed values of the head and aft pressure for $t > 1.0$ s that we noted in our discussion of case I. We mentioned previously that the computed head-to-aft-end pressure differential grows more slowly than the measurements indicate, and that this implies that the simulation increasingly underpredicts the amount of bore constriction during the period for $t = 1.0$ s to $t = 1.5$ s. Two factors that might contribute to this discrepancy are as follows. First, we have made no attempt to model corner erosion, i.e., the rounding of forward corners of propellant segments by the particle laden flow. This effect would tend to slow the rate of bore constriction. Since it appears that we already underpredict the rate of bore constriction, this might not seem to be a possible solution. However, the true situation is not that straightforward. We have found in our various SRMU simulations that a lower modulus tends to increase the head-to-aft pressure differential (by increasing the bore constriction rate) and to move the failure forward in time. For example, if we employ a somewhat lower modulus than the case I

modulus, we would expect to get a simulation where the head-to-aft pressure differential would be wider (i.e., in better agreement with the data), but the failure would have occurred earlier (i.e., worse agreement). Perhaps the inclusion of corner erosion in our model would help solve this dilemma. Second, our idealized deformed propellant shape (see Fig. 4) ignores the extent to which the propellant "bends over" at the corner. This approximation tends to cause an overprediction of the pressure differential at the corner, just as ignoring corner erosion does. An improved grid-generation component would remove this problem.

Acknowledgments

The authors would like to acknowledge N. R. Patel, S. H. Yang, and Y. S. Pan of The Aerospace Corporation for their assistance in generating structural influence coefficients.

References

[1]Romine, G. L., Huseman, P. G., and Sowers, G. F., "Stability Analysis of the SRMU PQM-1 Test Firing," 28th JANNAF Combustion Meeting, Brooks AFB, TX, Oct.–Nov. 1991.

[2]Chang, I-S., Patel, N. R., and Yang, S. H., "Titan IV SRMU Anomaly and Redesign Analyses," AIAA Paper 94-3284, June 1994.

[3]Glick, R. L., Caveny, L. H., and Thurman, J. L., "Internal Ballistics of Slotted-Tube Solid Propellant Rocket Motors," *Journal of Spacecraft and Rockets*, Vol. 4, No. 4, 1967, pp. 525–530.

[4]Johnston, W. A., "A Numerical Procedure for the Analysis of the Internal Flow in a Solid Rocket Motor During the Ignition Transient Period," AIAA Paper 91-1655, June 1991.

[5]Ton, V. T., Wang, J. C. T., and Widhopf, G. F., "Segmented Solid Rocket Motor Internal Flow Simulations," AIAA Paper 90-0683, Jan. 1990.

[6]Patel, N. R., and Yang, S. H., personal communication, The Aerospace Corp., Los Angeles, CA, 1991.

[7]Harten, A., "High Resolution Schemes for Hyperbolic Conservation Laws," *Journal of Computational Physics*, Vol. 49, No. 3, 1983, pp. 357–393.

[8]Wang, J. C. T., and Widhopf, G. F., "A High-Resolution TVD Finite Volume Scheme for the Euler Equations in Conservation Form," *Journal of Computational Physics*, Vol. 84, No. 1, 1989, pp. 145–173.

[9]*ABAQUS, Version 4.8, User's Manual*, Hibbit, Karlson and Sorensen, Inc., Palo Alto, CA, 1989.

[10]Johnston, W. A., "A Computational Fluid Dynamics Analysis of the Internal Flow in a Titan SRMU," AIAA Paper 90-2079, July 1990.

[11]"Two-Dimensional, Unsteady Flow Field Computer Program; User's Manual," Lockheed Missiles and Space Co., LMSC-D053117, Sunnyvale, CA, Sept. 1970.

[12]"Engineering Methods for Grain Structural Integrity Analysis," Lockheed Propulsion Co., LPC Rept. 578/556-F-3, Redlands, CA, May 1963.

[13]Christensen, L. W., private communication, Hercules Corp., Magna, UT, Nov. 4, 1991.

[14]"TITAN IV SRMU, Preliminary Design Review," Hercules Corp., Magna, UT, Feb. 1989.

[15]Kallmeyer, T. E., and Sayer, L. H., "Differences Between Actual and Predicted Pressure—Time Histories of Solid Rocket Motors," AIAA Paper 82-1094, June 1982.

[16]Johnston, W. A., "A Method for Reducing Stagnation Pressure Losses in Segmented Solid Rocket Motors," *Journal of Propulsion and Power*, Vol. 8, No. 3, 1992, pp. 720, 721.